Efficient transformation and elimination of roxarsone and its metabolites by a new α-FeOOH@GCA activating persulfate system under UV irradiation with subsequent As(V) recovery

Shanshan Su[a], Chengjin Cao[a], Yaping Zhao[a,*], Dionysios D. Dionysiou[b,*]

[a] School of Ecological and Environmental Sciences, Shanghai Key laboratory for Urban Ecological Process and Eco-Restoration, East China Normal University, and Institute of Eco-Chongming, Shanghai, 200062, China
[b] Environmental Engineering and Science Program, Department of Chemical and Environmental Engineering (ChEE), University of Cincinnati, Cincinnati, OH, 45221-0012, USA

ABSTRACT

Roxarsone (ROX) is extensively used as a feed additive which tends to leave toxic inorganic arsenic (As) in the natural environment. A composite of reduced graphene oxide and carbon nanotubes was impregnated with goethite designated as α-FeOOH@GCA and tested as an integrated catalyst and adsorbent for ROX decontamination. Nearly 100% of the ROX was transformed in α-FeOOH@GCA activating persulfate (PS) under UV_{365} irradiation system at relatively low dosage of the α-FeOOH@GCA catalyst (250 mg L^{-1}) in 120 min. The As(V) released in the ROX oxidation was simultaneously adsorbed onto the surface of the α-FeOOH@GCA. A possible ROX transformation pathway is proposed. The As(V) adsorbed on catalyst was recovered and used to form an efficient Ag_3AsO_4 photocatalyst. This work further extends the oxidation-adsorption technology in solving organoarsenical contamination without producing secondary pollution.

1. Introduction

Aromatic organoarsenics such as roxarsone (3-nitro-4-hydroxy benzene arsenic acid, ROX) are widely used in animal husbandry [1] as feed additives to improve meat yield, control parasites and improve animals' appearance [2,3]. The assimilation of organoarsenic in livestock appears to be extremely low. Most of it is excreted chemically unchanged and finally enters the environment through poultry litter [4]. In the environment, organoarsenic can be converted into species such as dimethylarsenic acid (DMA) and more toxic inorganic arsenic compounds including arsenates (As(V)) and arsenites (As(III)) through biotic and abiotic transformation under anaerobic conditions [1,5–7]. Organoarsenics are reported to be highly mobile and water soluble [8,9]. As a result, ROX and its degrdation products co-exist in the environment [10] and penetrate into groundwater [11] or accumulate in soils [12] and plants [13]. Ultimately, human beings are exposed [3,14–16,17]. ROX has been forbidden from the markets of the European Union and the U.S. since 1999 and 2013, respectively [11,13]. However, these feed additives are still being sold in many developing countries, including China and India [18].

The treatment of inorganic arsenic compounds has received much attention, but there have been few studies of their removal from the environment. A group led by Zheng studied the adsorption and photocatalytic oxidation of ROX on TiO_2 and demonstrated that hydroxyl radical plays the dominant role in the decomposition of ROX to As(V) [19]. Xie and his colleagues proposed a method that involves oxidation of arsanilic acid (p-ASA) through a Fenton process and removal of arsenate by forming an Fe-containing precipitate [9]. A group led by Li examined the efficiency of p-ASA photo-transformation [20], and Hu's group has shown that ROX can be efficiently oxidized to As(V) via a homogeneous Fenton reaction in a glow discharge plasma. The resulting inorganic arsenic can be immobilized by precipitating with Fe (III) ions [21]. Wang and his colleagues studied the adsorption and degradation of p-ASA on the surface of δ-MnO$_2$ which should be highly-relevant to arsenic soil pollution [18]. According to research by Shi [24], ROX can be converted into 4-hydroxy-3-aminophenylarsonic acid using electrochemical stimulation, which slowly decomposes to form As (III) as carbon sources are depleted under anaerobic conditions. However, in those oxidation processes, the inorganic arsenic products formed remain in the solution or in the arsenic-bearing precipitate. The complete removal of As(V) species needs subsequent post-treatment, a topic which has received little attention. Recycling of inorganic arsenic

is of interest because the disposal of arsenic remains an unsolved toxicological and environmental problem. A more efficient and environment-friendly integrated degradation of organoarsenic species which immobilizes the inorganic arsenic formed and recycles stripped arsenic is urgently needed.

Sulfate radical ($SO_4^{\cdot-}$) oxidation is a powerful advanced oxidation process (AOP) for remediating environmental contamination involving organics [22–24]. Persulfate (PS) can be activated using ultraviolet (UV) light, transition metals, heat, ultrasound (US), or certain chemicals [25–27]. Iron-based transition-metal catalysts are among the most popular heterogeneous activators for AOPs due to their geological abundance and low environmental impact [26]. For example, the amorphous alloy of Fe-based metallic glass $Fe_{78}Si_9B_{13}$ was proved to be a highly efficient Fenton-like catalyst in producing hydroxyl radicals and degrading cibacron brilliant red 3B-A dye under visible light irradiation [28–31]. Fe-based Metal Organic Frameworks (MOFs) have demonstrated excellent photocatalytic behavior in CO_2 reduction or adsorption and photocatalytic degradation of tetracycline [32,33]. Zero-valent iron was employed as a PS heterogeneous activator and demonstrated high removal of polycyclic aromatic hydrocarbons (PAHs) [34]. Among them, goethite (α-FeOOH) has been demonstrated to be an efficient heterogeneous catalyst for Fenton-like reactions [35], photocatalytic reactions [36,37] and electrocatalytic applications [38]. Goethite is abundant, easily accessibility, of low toxicity, with relatively high specific surface area and good stability [39–41]. However, the catalytic degradation efficiency of pristine α-FeOOH is inhibited by its small particle size and easy aggregation, which impede its reactivity and make it difficult to recover. In order to improve the material's catalytic properties, α-FeOOH nanocomposites have been designed through their interaction with appropriate carriers. Activated carbon, activated alumina, clay, zeolite resin, silica and other supports have been tested.

Compared with traditional supports, carbon-based aerogels offer lower density, chemical stability and excellent electron conductivity. Electrons can move rapidly through the aerogel's 3D porous framework. The hierarchical structure of a carbon-based aerogel can provide a substrate with high and very accessible surface area for adsorption [42]. Those special properties have made carbon-based materials superior catalyst supports. The development of graphene oxide (GO) and carbon nano-tubes (CNTs) has promoted the development of carriers in the environment and energy fields. GO has a relatively large specific surface area and oxygen-containing groups. It is used as a fairly good support for catalyst centers [43]. However, GO tends to aggregate during its preparation through strong π-π interaction between organic substrates and individual sheets [44]. CNTs can be used as a spacer material entangling with GO nano-sheets and converting them to a 3D, self-supporting macrostructure aerogel [43,45]. The role of GO-CNT aerogel composite matrix is its ability to enhance the desirable catalytic activity and accelerate the mass transfer of substrate when interacting with pristine α-FeOOH [46].

The aims of this study were (i) to synthesize bi-functional α-FeOOH@GCA composites with catalytic oxidation and adsorption properties; (ii) to test them in the in-situ catalytic oxidation of ROX and for adsorption of As(V) formed through the activating persulfate under UV light process (designed as α-FeOOH@GCA/PS/UV system); (iii) to explore the catalytic ROX oxidation mechanism; and (iv) to find a sustainable way to deal with the As(V) stripped from the surface of α-FeOOH@GCA. The objective was to propose a new way of completely removing organoarsenic from water without requiring disposal of the inorganic arsenic by-products formed.

2. Experimental

2.1. Chemicals

Roxarsone ($C_6H_6AsNO_6$, MW = 263.04, 99%) was purchased from

Alfa Aesar Ltd. (Shanghai, China). Hydroxyl multi-wall carbon nanotubes were purchased from Chengdu Organic Chemistry (Chengdu, China) and natural graphite was bought from Guangfu Chemicals (Tianjin, China). Ferrous sulphate ($FeSO_4 \cdot 7H_2O$), was purchased from Sinopharm Chemical Reagent Ltd. (Shanghai, China). Coumarin, 7-hydroxycoumarin and potassium persulfate were purchased from Aladdin Ltd. (Shanghai, China). Tetranitromethane (TNM) and 5,5-Dimethyl-1-pyrrolidine N-oxide (DMPO, 97%) were purchased from Sigma-Aldrich (Shanghai, China).

2.2. Characterization

The morphology of α-FeOOH@GCA was characterized with field emission scanning electron microscopy (FE-SEM, JEOL S-4800, Hitachi, Japan) and transmission electron microscopy (TEM, JEOL JEM-2100 F, Hitachi, Japan), respectively. The crystalline phase of α-FeOOH@GCA was analyzed with Ultima IV type X-ray diffractometer (XRD, Rigaku D/Max-2500, Japan) employing Cu-Kα as source of radiation, $\lambda = 1.5406$ Å at a scan speed of $10°$ min^{-1} over an angular range between $5°$ to $70°$. The functional groups of α-FeOOH@GCA were examined by a Bruker Fourier transform infrared spectrophotometer (FTIR, Finnigan Nicolet Nexus 600, Thermo, USA) with the KBr pellet. The surface elemental compositions of α-FeOOH@GCA were determined by X-ray photoelectron spectroscopy (XPS) acquired with an Axis Ultra spectrometer (Kratos, Japan).

2.3. ROX degradation experiments

α-FeOOH@GCA was prepared using published methods [46]. In brief, the 400 ml of uniformed dispersion containing 0.400 g of GO, 0.172 g of CNTs and 7.228 g of $FeSO_4 \cdot 7H_2O$ was sonicated and then hydrolyzed in an oil bath at 95 °C for 6 h. The as-formed α-FeOOH@GCA hydrogel was repeatedly washed with deionized water and freeze-dried.

The degradation experiments were performed in borosilicate evaporating dishes. A 100 W high-pressure Hg lamp ($\lambda_{max} = 365$ nm, Phillips GGY100Z) was used to irradiate the samples at an intensity of 1.4 mW cm^{-2}. Typically, 50 mg of α-FeOOH@GCA (250 mg L^{-1}) and 0.162 g of $K_2S_2O_8$ (3 mM) were dispersed into 200 mL ROX solution with an initial concentration of 20 mg-As L^{-1} and strring at 25 °C without adjusting solution pH (3.58). Other experiments were carried out according to above procedures either in presence/absence of PS or UV irradiation. At predetermined time intervals, samples of about 2 mL were extracted and filtered through a 0.22 μm membrane filter. The concentration of ROX in the filtrate was measured using liquid chromatography (SPD-20 A, Shimadzu, Japan) with a C18 reversed-phase column (5 μm, 4.6 × 150 mm, Agilent, USA). The detection wavelength was 266 nm and the column temperature was maintained at 25 °C. The mobile phase was acetonitrile and ultrapure water in a volume ratio of 6:4 at a flow rate of 0.4 ml min^{-1}. The ROX degradation ratio was then calculated as

$$\text{Degradation ratio (\%)} = 100 \times (C_0 - C_t)/C_0 \qquad (1)$$

where C_0 and C_t are the concentrations of ROX at times 0 and t, respectively. The persulfate concentration was determind by a spectrophotometry using a modified iodometric titration method [47]. The mineralization of ROX was determined with a total organic carbon (TOC) analyzer (TOC-5050, Shimazdu, Japan). The ROX degradation intermediates adsorbed on the surface of the α-FeOOH@GCA were identified with time-of-flightsecondary ion mass spectrometry (TOF-SIMS) (IONTOF GmbH, Germany) with a Bi liquid metal ion gun as the primary ion source. A 30 keV Bi^+ beam with a pulsed primary ion current was used in burst mode to obtain TOF-SIMS. The analysis area was 500 × 500 $μm^2$. The dose density of Bi^{3+} ions was 8.18×10^{11} cm^{-2}. With the finely-focused Bi^{3+} primary ion gun at 30 keV and
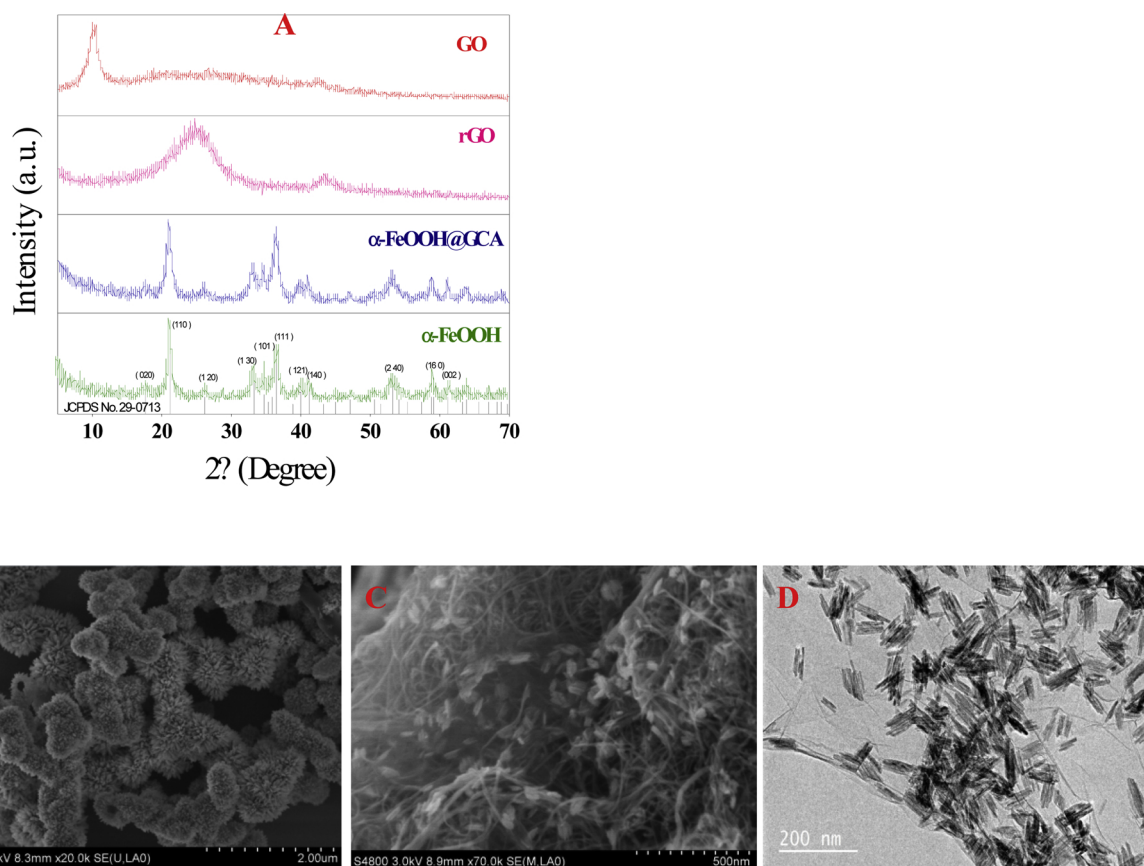
Fig. 1. (A) X-ray diffraction spectra for GO, reduced GO, α-FeOOH@GCA and pristine α-FeOOH. (B) SEM image of α-FeOOH. (C) SEM image of α-FeOOH@GCA. (D) TEM image of α-FeOOH@GCA.

various currents, both the negative and positive spectra were obtained. The beam scanned over areas of 30×30 μm^2 and 24×24 μm^2 to obtain ion images. As for the mineralization product of ROX, the arsenic molybdenum blue spectrophotometric method was applied to determine the concentration of As(V) or desorbed As(V) (UV-1102, Tianmei Tech Ltd., China). SA-10 atomic fluorescence speciation analyzer (AFS-9230/SA-10) was used to separate and measure the concentration of As(III) and As(V). All experiments were done in triplicate.

The stability of α-FeOOH@GCA was evaluated by conducting six consecutive catalytic cycles. The α-FeOOH@GCA was separated from the α-FeOOH@GCA/PS/UV system by centrifugation after each cycle; and respectively treated with 0.1 M NaOH, 0.1 M HCl and distilled water to remove the adsorbed As(V) and other by-products.

2.4. Radical quenching experiments

To investigate the reactive oxygen species involved in the α-FeOOH@GCA/PS/UV system, methanol (MeOH), *tert*-butyl alcohol (*t*-BuOH), KI and ascorbic acid (AA) were used as scavengers of hydroxyl radical (˙OH), sulfate radical (SO$_4$˙$^-$) in the solution, SO$_4$˙$^-$ on the surface of the catalyst and superoxide radical (O$_2$˙$^-$), respectively. The quantitative detection of the ˙OH and O$_2$˙$^-$ radicals employed radical trapping techniques. Coumarin and TNM were reacted with ˙OH and O$_2$˙$^-$ radicals, respectively. The 7-hydroxycoumarin reaction product was quantified by fluorescence spectrometry at an excitation wavelength of 332 nm [48] (Hitachi F-4500, Japan). Nitroform, the main product of the reaction between O$_2$˙$^-$ and TNM, was measured at 350 nm through a UV–vis spectrophotometer [49]. Electron paramagnetic resonance (EPR) spectra were used to confirm the presence of ˙OH, SO$_4$˙$^-$ and O$_2$˙$^-$ radicals in the system. The spectrometry (JES-FA200, Bruker, Germany) was performed at a resonance frequency of

9054 MHz with a microwave power of 0.998 mW at a modulation frequency of 100 kHz with modulation amplitude of 2 and a sweep width of 5 m T. The time constant was 0.03 s, with a sweep time of 1.0 min for the ˙OH and SO$_4$˙$^-$ radicals and a resonance frequency of 9439 MHz. The sweep time was 30 s for the O$_2$˙$^-$ radicals. The radical spin-trapping reagent was DMPO (100 mM) in water solution.

2.5. Recovery of As(v) formed as Ag$_3$AsO$_4$ photocatalyst

The Ag$_3$AsO$_4$ photocatalyst was prepared using the method described by Hott [50]. The arsenic-adsorbed α-FeOOH@GCA was separated from the α-FeOOH@GCA/PS/UV system by centrifugation and stripped with 0.1 M NaOH to obtain As(V). The As(V) solution was separated from α-FeOOH@GCA and the pH of the As(V) solution was adjusted to 5.0 using 0.1 M HNO$_3$. AgNO$_3$ was dropwised into As(V) soultion to form a reddish-brown silver arsenate (Ag$_3$AsO$_4$) precipitate which was separated and dried at room temperature.

The photocatalytic activity of the as-obtained Ag$_3$AsO$_4$ was evaluated through degradation of four kinds of dyes, one endocrine disrupting compound, bisphenol A (BPA), 4-nitrophenol (4-NP) and phenol. The dyes were the cationic dyes methylene blue (MB) and rhodamine B (RhB), and the anionic dyes orange II (OII) and orange G (OG). The photocatalytic degradation experiments were carried out according to the ROX degradation procedures aforementioned. Typically, 50 mg of Ag$_3$AsO$_4$ was added to 200 mL of a solution of 5 mg L^{-1} of the organic contaminant. The suspensions were stirred and irradiated with UV light. The concentrations of the organics were determined by UV–vis spectrophotometry or HPLC.

3. Results and discussion

3.1. Structure properties of α-FeOOH@GCA

The self-assembled α-FeOOH@GCA macrostructures were fabricated in hopes of enhancing the catalytic activity of α-FeOOH [46]. According to previous report [46], the crystalline structure and morphologies of as-prepared α-FeOOH or α-FeOOH@GCA were shown in Fig. 1. The raft-like α-FeOOH nanorods with the average length of 50 nm were uniformly dispersed on the surface of GO-CNTs aerogel. The role of the GO-CNTs carrier is not just preventing agglomeration, but also for nanometrizing the structure of the α-FeOOH crystals and increasing the mass transfer of substrate. GO-CNTs carrier also provides enhanced electron transfer ability and catalytic activity due to formation of Fe-O-C bond between the interface of α-FeOOH and the GO-CNT structure [46]. In this work, α-FeOOH@GCA was tested as a bifunctional reagent combining catalytic and adsorption ability realizing ROX degradation- formed As(V) adsorption in α-FeOOH@GCA/PS/UV system.

3.2. ROX degradation under different conditions

The catalytic and adsorption activities of ROX in an α-FeOOH@GCA-catalyzed PS activation system were explored under UV irradiation. The removal of ROX under different conditions as a function of time is shown in Fig. 2A. The degradation ratio of ROX under UV photolysis (1.2%) or oxidation by PS in daylight (4.4%) was not significantly changed after 120 min. ROX is clearly very stable in water or soil under sunlight irradiation [36,51,52]. The photocatalytic degradation of ROX in the FeOOH@GCA/UV system (66%) was lower than in the α-FeOOH@GCA adsorption system (69%) after 120 min. The formation of As(V) from the degradation of ROX in FeOOH@GCA/ UV system was about 2.05 mg L^{-1}. The ROX degradation ratio in the PS/UV system increased steadily to 100% after 120 min with the

formation of stoichiometric amount of As(V) oxyanions in the solution. That was attributed to the SO$_4^{\cdot-}$ generated from photolytic activation of the PS [53]. The degradation ratio of ROX in the α-FeOOH@GCA/PS system increased sharply to 75% within 10 min and then gradually decreased to 58% after 120 min. That can be ascribed to the competition of released As(V) with ROX adsorbed on the surface of the α-FeOOH@GCA leading to a deterioration of the catalytic ability of As(V) adsorbed α-FeOOH@GCA. The degradation ratio of ROX in the α-FeOOH@GCA/PS/UV system can reach nearly 100% within 30 min before plateauing until 120 min, which is completely different from the ROX degradation in α-FeOOH@GCA/PS system. It shows that the complete conversion kinetics from ROX to As(V) in the α-FeOOH@GCA/PS/UV system is far faster than the exchange kinetics between adsorbed ROX and As(V) formed on the surface of α-FeOOH@GCA. While the conversion from ROX to As(V) in α-FeOOH@GCA/PS system after 10 min shows relatively slower degradation kinetics than the exchange kinetics between adsorbed ROX and the As(V) formed, the synergistic α-FeOOH@GCA/PS/UV system greatly enhances the ROX degradation kinetics, surpassing those of As (V) adsorption.

The adsorption of the target pollutant onto the catalyst surface is key to the catalytic degradation process. Compared with the adsorption ratio of ROX on α-FeOOH@GCA, the removal ratio of ROX in the α-FeOOH@GCA/UV system is lower; while the removal ratio of ROX with α-FeOOH@GCA/PS decreases with reaction time. That shows a gradual release of ROX from the α-FeOOH@GCA surface due to competition of As(V) released from ROX degradation. To shed light on this phenomenon, competitive adsorption of ROX and the main degradation product As(V) on α-FeOOH@GCA is shown in Fig. 2B. In a single adsorption system, the removal ratios of ROX and As(V) were 69.0% and 32.9%, respectively. The adsorption ratio of ROX decreased from 69.0% to 51.2% in the presence of same concentration of As(V), while the adsorption ratio of As(V) decreased from 32.9% to 27.6% in presence of ROX. These results show that As(V) has higher affinity or stronger
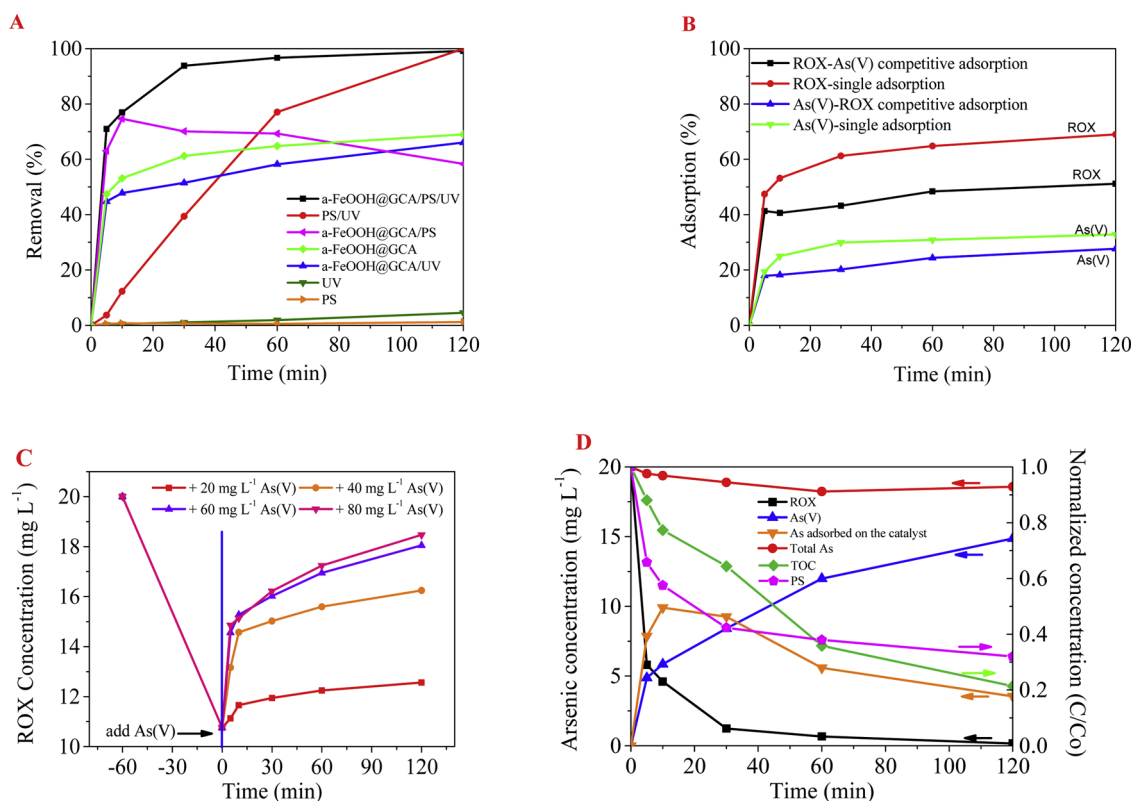

Fig. 2. (A) Removal of ROX under different experimental conditions. (B) Competition between As(V) and ROX adsorption. (C) Desorption of ROX with the addition of As(V). (D) The changes in ROX, As(V), TOC and PS with time.

binding ability with α-FeOOH@GCA than that of ROX. The desorption of ROX pre-adsorbed on α-FeOOH@GCA in the presence of As(V) was also investigated, and the results are shown in Fig. 2C. When the adsorption and desorption of ROX on α-FeOOH@GCA reached equilibrium, the residual concentration of ROX had increased from 6.5 to 7.5 or 18.5 mg L^{-1} after adding 20 or 80 mg L^{-1} As(V). The desorption of ROX from the surface of α-FeOOH@GCA increases with the increase of As(V) concentration in this system. It shows that the presence of target degradation product As(V) competes for adsorption sites with ROX, leading to the desorption or releasing of the previously-adsorbed ROX from the surface of α-FeOOH@GCA, which can explain the lower removal ratio of ROX in the α-FeOOH@GCA/UV or α-FeOOH@GCA/PS system.

The mineralization of ROX in the α-FeOOH@GCA/PS/UV system was also studied, and the results are shown in Fig. 2D. Both the formation of As(V) oxyanions and the decreasing ROX concentration in the α-FeOOH@GCA/PS/UV system with time demonstrate the complete breaking of As-C bonds in the ROX. The concentration of ROX in solution gradually decreased from an initial 20 mg L^{-1} to nearly zero, and the concentration of released As(V) in the solution increased steadily to 14.9 mg L^{-1}, though not to 20 mg L^{-1} due to the in-situ adsorption of part of the As(V) formed by the α-FeOOH@GCA. The downward trend of the system's TOC is similar to that of the ROX. The decrease in solution TOC may be the result of both ROX mineralization and the adsorption of organic by-products [9]. An arsenic mass balance during the degradation process was also calculated. The total arsenic species adsorbed on the surface of α-FeOOH@GCA nearly reached 50% within 10 min but then slowly decreased to 18% after 120 min, leaving mainly As(V) anion species at the end of the degradation. The ROX was entirely transformed into As(V) in this process after 120 min leading the concentration of As(V) to gradually increase to 14.8 mg L^{-1}. In addition, almost no As(III) was detected in the solution or on the surface of the α-FeOOH@GCA due to the strong oxidizing conditions. The total arsenic mass balance has a slight downward trend, which may be unavoidable due to the catalyst and liquid loss during each sampling or because not all adsorbed arsenic species could be recovered. About 80% PS can be effectively activated in the α-FeOOH@GC/PS/UV system after 120 min. The reduction in PS concentration represents the production of free active species such as the SO$_4^{\cdot-}$ and ˙OH radicals [54]. The observed decrease in PS is consistent with the trends in ROX degradation and TOC reduction.

3.3. The effect of initial pH

pH is a significant factor which influences the interface properties of the catalyst, substrates and the distribution of free radicals in AOPs. The effect of initial pH (written as pH$_0$) on ROX degradation in the α-

FeOOH@GCA/PS/UV system is illustrated in Fig. 3. The degradation ratio of ROX (99.39%) was most significant at initial pH 2.98. The degradation ratio decreased with increasing initial pH from 2.98 to 11.01, which is consistent with the observations of previous studies on the removal of refractory organics in heterogeneous catalyst and persulfate oxidation systems [54,55]. An obvious reduction in pH value was observed during ROX degradation reaction, i.e. the final solution pH was about 2.10 when the initial pH was in the range from 2.98 to 9.65; while the final solution pH was about 8.50 when the initial pH was 11.01. From the pH values monitored before and after the reaction, it can be concluded that in the cases of initial pH from 2.98 to 9.65, SO$_4^{\cdot-}$ radicals are the major active species mostly under acidic conditions during the reaction. However, when initial pH was 11.01, ˙OH radicals was the dominant active species under alkaline conditions [26]. The zero point charge (pH$_{ZPC}$) of α-FeOOH@GCA is about 3.4 [46]. The surface of α-FeOOH@GCA is positively charged when pH was 2.98, which could enhance the adsorption between α-FeOOH@GCA and ROX due to electrostatic attraction. Thus, the degradation efficiency of ROX was improved. However, the surface of α-FeOOH@GCA is negatively charged at a pH higher than 3.4, which is unfavorable for the adsorption of negatively charged ROX species due to electrostatic repulsion. In addition, the adsorption of S$_2$O$_8^{2-}$ anions on the negatively charged surface of α-FeOOH@GCA would also be hindered due to electrostatic repulsion, leading to reduced generatation of active radicals and gradually declined ROX degradation efficiency in α-FeOOH@GCA/PS/UV system.

3.4. Durability of α-FeOOH@GCA

The stability of α-FeOOH@GCA was evaluated by evaluating its ROX degradation efficiency in an α-FeOOH@GCA/PS/UV system over six consecutive catalytic cycles. The result is shown in Fig. 4A. From Fig. 4A, it can be seen that the ROX degradation ratio in α-FeOOH@GCA/PS/UV system was gradually deteriorated after each cycle without desorption of adsorbed As(V) from catalyst which may due to the deactivation of catalyst and some loss of α-FeOOH@GCA during the elution procedures [56,57]. Comparably, the ROX degradation ratio in α-FeOOH@GCA/PS/UV system remained stable after each cycle with desorption of As(V) from the surface of the catalyst indicating the catalytic property of α-FeOOH@GCA was relatively stable. In the first cycle, the desorbed As species from the fresh catalyst was about 3.6 mg L^{-1}; while in the sixth cycle, the desorbed As species from catalyst was about 3.4 mg L^{-1}. This result indicates a strong deactivation of α-FeOOH@GCA catalytic activity mainly owing to the adsorption of large amount of As(V). Besides, the influence of adsorption of PS, reactants or by-products onto the catalyst's surface also cannot be neglected. Total iron content can also indicate catalyst
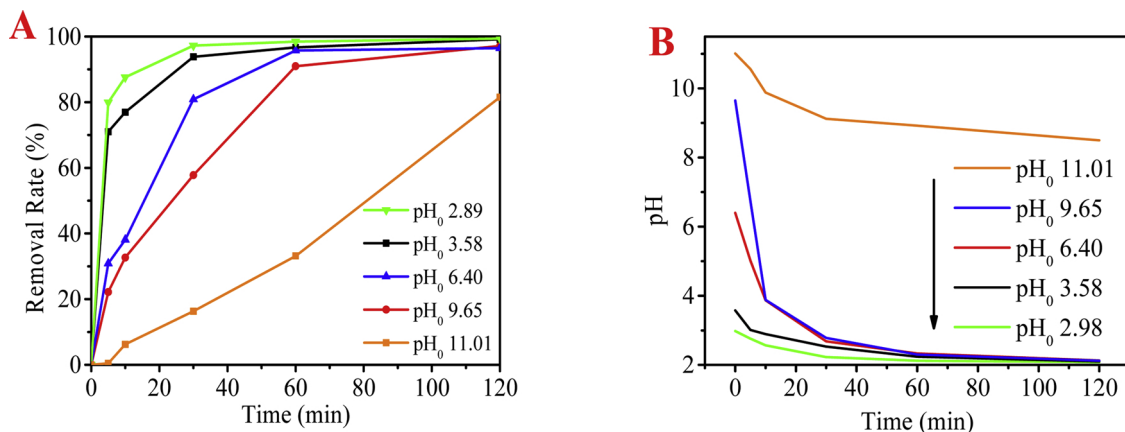

Fig. 3. Degradation of ROX in an α-FeOOH@GCA/PS/UV system at different initial pH (A) and pH evolution under different initial pH (B).
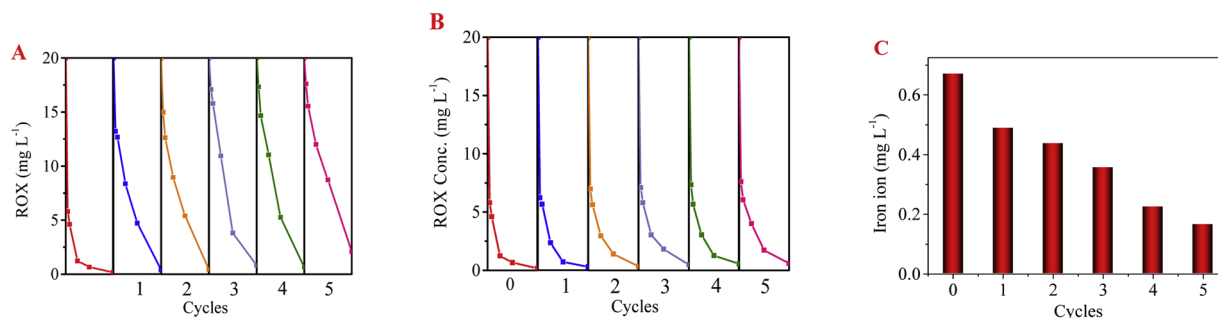
Fig. 4. ROX degradation without (A) and with (B) desorption of adsorbed As(V) from catalyst, and total iron leakage (C) in an α-FeOOH@GCA/PS/UV system over 6 cycles.

stability [57]. Fig. 4B shows that the dissolved total iron content dropped from 0.67 to 0.16 mg L^{-1} after six reuse cycles. That total iron leakage is below the EU's discharge standards for Fe (2 mg L^{-1}), so the process would not produce secondary pollution [58].

3.5. The mechanism of ROX degradation

3.5.1. The free radicals involved

Radical quenching experiments were performed with the results shown in Fig. 5. Previous studies have indicated that $SO_4^{\cdot-}$ and $O_2^{\cdot-}$ radicals can be generated after activating PS [59]. In most cases, and especially under alkaline conditions, $SO_4^{\cdot-}$ can further react with H_2O or OH^- resulting in the formation of ·OH radicals [60,61]. The presence of $SO_4^{\cdot-}$, ·OH and $O_2^{\cdot-}$ might be anticipated to be responsible for ROX degradation in an α-FeOOH@GCA/PS/UV system. In this work, methanol, *t*-BuOH, KI and AA were employed as radical scavengers of ·OH, $SO_4^{\cdot-}$ (in the solution), $SO_4^{\cdot-}$ (on the surface of catalyst) and $O_2^{\cdot-}$,

respectively [62]. MeOH can react readily with both $SO_4^{\cdot-}$ (3.2×10^6 M^{-1} s^{-1}) and ·OH (9.7×10^8 M^{-1} s^{-1}). However, *t*-BuOH can react much faster with ·OH (3.8–7.6×10^8 M^{-1} s^{-1}) than with $SO_4^{\cdot-}$ (4–9.1×10^5 M^{-1} s^{-1}) [63]. In Fig. 5A, *t*-BuOH just has a slight inhibiting effect on ROX degradation in an α-FeOOH@GCA/PS/UV system. *t*-BuOH is of course hydrophilic, so it is more likely to react with free radicals in the liquid phase in preference to free radicals bound to the catalyst surface [55,64]. MeOH has an obviously greater inhibiting effect than *t*-BuOH. In order to study the function of $O_2^{\cdot-}$ radicals generated from the dissolved oxygen [65], AA was added to the solution. As shown in Fig. 5A, the resulting decrease in $O_2^{\cdot-}$ radicals did inhibit the degradation of ROX to some extent.

To further verify the process, ·OH and $O_2^{\cdot-}$ radical concentrations were determined. The results are shown in Fig. 5B. The maximum concentration of ·OH radical adducts was 0.58 mM after 120 min. In fact, the majority of the ·OH formed should have come from the oxidation of $SO_4^{\cdot-}$ radicals rather than the direct formation of ·OH, which

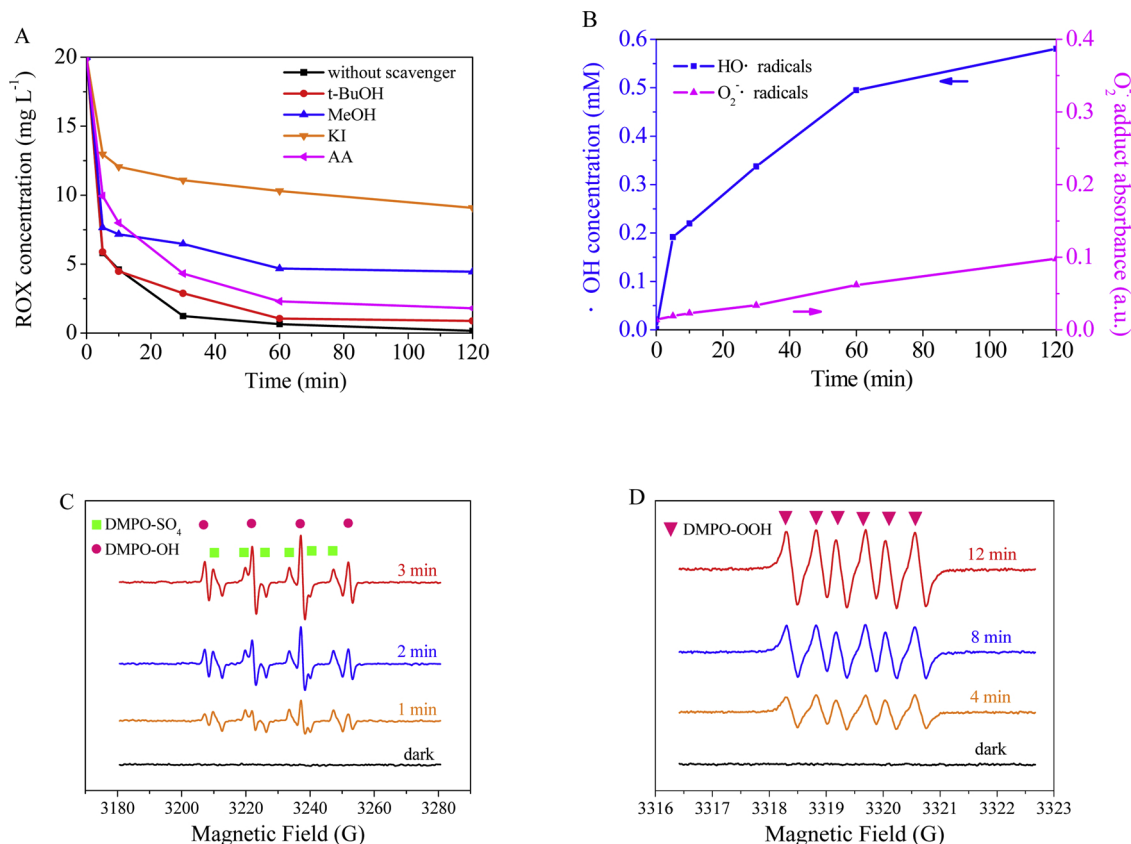**Fig. 5.** (A) Degradation of ROX in presence of radical scavengers, (B) quantative generation of ·OH and $O_2^{\cdot-}$ radicals, (C) EPR spectra of DMPO-SO$_4$ or DMPO−OH and (D) DMPO−OOH in the α-FeOOH@GCA/PS/UV system with time.

was confirmed from the *t*-BuOH quenching experiment. The absorbance of trinitromethane formed by oxidation TNM by $O_2^{\cdot -}$ radicals increased with time. However, $O_2^{\cdot -}$ (E = 1.3 V vs. NHE) is a relatively ineffective oxidant for organic contaminants [62]. So $SO_4^{\cdot -}$ rather than $^{\cdot}OH$ or $O_2^{\cdot -}$ in the bulk solution was the dominant active species in this system. Lin Tang and his coauthors have also demonstrated the existence of $SO_4^{\cdot -}$ and $^{\cdot}OH$ radicals and that they make a major contribution to the removal of 2,4-dichlorophenol in a mesoporous carbon/persulfate system [66]. It has been reported that KI is as an efficient inhibitor of surface-bound $SO_4^{\cdot -}$ and $^{\cdot}OH$ [67,68]. From Fig. 5A, it is obvious that the ROX degradation efficiency has been remarkably decreased (from 99.2% to 49.0%) after the addition of KI. Therefore, the results suggest that surface-bound $SO_4^{\cdot -}$ radicals were the dominant reactive oxygen species responsible for the degradation of ROX in the α-FeOOH@GCA/PS/UV system.

Electron paramagnetic resonance (EPR) spectra were recorded to further confirm the presence of the dominant free radicals and to better elucidate the mechanism of PS activation. As shown in Fig. 5C, the appearance of DMPO-SO₄ signals (six lines with relative intensities of 1:1:1:1:1:1) and DMPO−OH signals (four lines with intensities of 1:2:2:1) can be ascribed to the formation of $SO_4^{\cdot -}$ and $^{\cdot}OH$ radicals, respectively. The hyperfine splitting constants for DMPO-SO₄ were $a_N = 13.2$ G, $a_H = 9.6$ G, $a_H = 1.48$ G and $a_H = 0.77$ G, and for DMPO−OH they were $a_N = a_H = 14.8$ G. Those values agree well with some previously reported [66,69]. In Fig. 5D, DMPO−OOH also appeared in the α-FeOOH@GCA/PS/UV system with the six characteristic peaks, further indicating the formation of $O_2^{\cdot -}$ radicals. The signals suggest that $SO_4^{\cdot -}$, $^{\cdot}OH$ and $O_2^{\cdot -}$ were the dominant free radicals in the α-FeOOH@GCA/PS/UV system playing a significant role in ROX degradation. This agrees with the quenching results. In addition, the peak intensities of DMPO-SO₄, DMPO−OH and DMPO−OOH increased with the reaction time, increasing radical concentrations in this PS activation system.

3.5.2. ROX evolution

The UV–vis absorption changes of ROX in α-FeOOH@GCA/PS/UV system with time are shown in Fig. 6. The main peaks at 340 and 270 nm were assigned to the aromatic ring [2,70]. The absorption band at 254 nm mainly originates from the benzene or unsaturated carbon bonds [71]. The intensity of these absorption bands decreased with reaction time. After 120 min of degradation, the absorption bands around 270 and 340 nm had become negligible. This indicates the complete cleavage of the nitro, As-C bonds and the aromatic rings of ROX due to the oxidation in thisα-FeOOH@GCA/PS/UV system. The ROX was finally decomposed into As(V) anions, organic by-products and nitrates. As reported elsewhere, photodegradation of roxarsone in
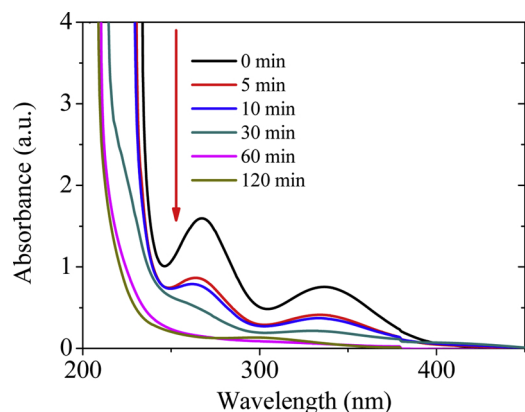

Fig. 6. The evolution of the UV–vis spectra during the degradation of ROX in the α-FeOOH@GCA/PS/UV system with time (with the steric structure of ROX inset).

poultry litter leachates also experienced the same rapidly oxidation and the cleavage pathway of As-C and aromatic rings [72].

Usually, the degradation intermediates are identified using HPLC coupled with a mass spectrometer. In this study, to inspect the changes in the molecular structure of the ROX, TOF-SIMS was applied instead in an attempt to better elucidate the surface distribution of the elements and degradation intermediates. Fig. 7A-B shows TOF-SIMS images of FeO_2^- and AsO_2^- in negative ion mode and of Fe^+ and As^+ in positive ion mode of α-FeOOH@GCA surface over a $30 \times 30 \ \mu m^2$ area. The outline images of single α-FeOOH@GCA particles in negative or positive ion mode can be clearly observed in the total element spectra or in the silicon substrate's spectra. The negative ion mode image of arsenic in Fig. 7A offers powerful evidence of the adsorption of As-containing intermediates and by-products on the surface of the α-FeOOH@GCA particles. The positive ion mode image in Fig. 7B shows that iron is uniformly dispersed on the surface of the α-FeOOH@GCA particles, while arsenic is not observed. Negative and positive ion mode mass spectra of ROX degradation intermediates adsorbed on the surface of α-FeOOH@GCA in this system are shown in Fig. 7C-D. The mass spectra of α-FeOOH@GCA observed below $m/z = 100$ were mainly ascribed to O, C, Fe and As elements. Many other significant peaks due to hydrocarbon fragment impurities generated from the sample or the vacuum system were found in most of the TOF-SIMS spectra [73]. Similar to $^{\cdot}OH$, $SO_4^{\cdot -}$ radicals formed can react with organic matter through electron transfer, hydrogen extraction or addition reaction mechanisms. In this experiment the degradation involved first the cleavage of As-C bonds in the ROX ($m/z = 263$). That had faster degradation kinetics in the α-FeOOH@GCA/PS/UV system, resulting in the formation of by-products corresponding to $m/z = 139, 155, 126$ and 124. For example, $SO_4^{\cdot -}$ can react with aromatic compounds through an electron transfer chain reaction [74]. The cleavage of As-C bonds in the ROX molecule initiates with the oxidation of aromatic rings by $SO_4^{\cdot -}$ through a single electron transfer mechanism. That results in the formation of As(V) oxyanions and o-nitrophenol ($m/z = 139$). O-nitrophenol continues to be attacked by the radicals leading to the formation of hydroxyl-substituted phenolic compounds. The nitro group in the aromatic ring of o-nitrophenol is easily attacked by the radicals due to its strong electron receptor effect, which leads to the formation of hydroxyquinol. Hydroxyl in the aromatic ring takes part in the oxidation reaction and is converted to carbonyl. O-nitrophenol can at the same time react with $^{\cdot}OH$ to be converted into catechol ($m/z = 110$). Catechol can be oxidized to o-benzoquinone ($m/z = 108$), which further results in a ring opening reaction to form a series of short-chain carboxylic acids. Eventually, low molecular weight intermediates can be mineralized to CO_2 and H_2O providing the reaction time is sufficient. In Fig. S1, the HPLC-MS result shows the formation of by-products corresponding to $m/z = 280, 263, 235, 139, 126$ and 94, which were the same with the results obtained by TOF-SIMS analysis; by-products corresponding to $m/z = 184$ was reported to be dinitrophenol [3]; while other lower molecules with $m/z = 84$ and 60 were not identified. The proposed ROX degradation pathway based on these results is presented in Scheme 1. This result proves that the catalytic degradation of ROX is occurring on the surface of α-FeOOH@GCA, not just simple adsorption.

3.5.3. A proposed PS activation mechanism

Fourier-transform infrared absorption patterns for α-FeOOH@GCA before and after degradation/adsorption of ROX in the α-FeOOH@GCA/PS/UV system are presented in Fig. 8A. The strong peaks at 3154 cm^{-1} and 3455 cm^{-1} of α-FeOOH@GCA (curve A1 in Fig. 8A) are assigned to hydroxyl stretching in the α-FeOOH and the bending mode of water molecules on the catalyst [75,76]. The peaks at 1582 cm^{-1} and 1714 cm^{-1} are the stretching of aromatic rings and C=O bonds in the GO and CNTs [26]. The absorption band at around 1210 cm^{-1} can be ascribed to C–O stretching. The peak at 1132 cm^{-1} is attributed to the split asymmetric strong v_3 SO₄ mode that relates to a bidentate complex [77,78]. Some bands at 878 cm^{-1}, 787 cm^{-1} and 599 cm^{-1} can be
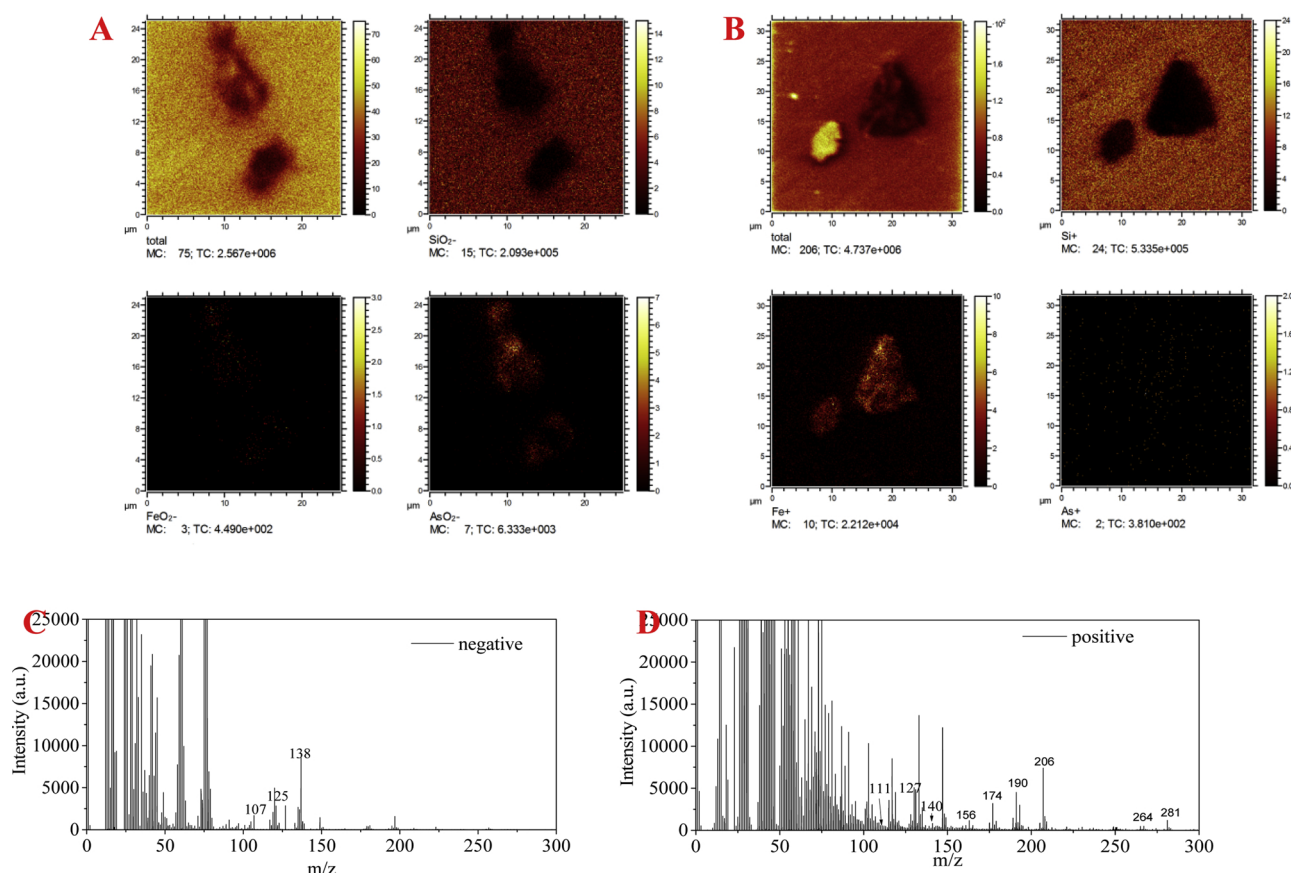
Fig. 7. (A) Negative and (B) positive ion mode TOF-SIMS elemental mappings of a single α-FeOOH@GCA particle; (C) Negative and (D) positive ion mode TOF-SIMS spectra of ROX degradation intermediates on the solid surface of α-FeOOH@GCA in the α-FeOOH@GCA/PS/UV system after 120 min.

attributed to Fe—O—H bending vibrations in the catalyst and Fe—O stretching modes [79,80].

After adsorption of ROX (curve A2 in Fig. 8A), the disappearance of the peak at 3455 cm^{-1} was attributed to the interaction between organoarsenic and the water molecules chelated with Fe [81]. The new peak at 841 cm^{-1} occurred due to the formation of As-O-Fe bonds [82] indicating ROX adsorbed on the surface of the α-FeOOH@GCA. The strong peaks at 1615 cm^{-1}, 1572 cm^{-1} and 1533 cm^{-1} are due to the stretching of aromatic rings in the ROX molecular structure [83–86]. The peaks of α-FeOOH@GCA shifted from 879 cm^{-1} to 841 cm^{-1} after ROX adsorption. Such a blue-shift indicates interaction between ROX and α-FeOOH on the surface of the α-FeOOH@GCA.

The spectrum of As(V) adsorption (curve A3 in Fig. 8A) was detected to reconfirm the transfer from ROX to As(V) on the surface of α-FeOOH@GCA in this system. After the adsorption of As(V), increased intensity of bands at 878 cm^{-1} and 787 cm^{-1} was observed; these bands have been assigned to the symmetric stretching vibration of As—O—Fe interaction [87,88]. The peaks at 1132 cm^{-1} disappeared in this spectrum, which could be explained by the participation of SO_4^{2-} in anion-exchange reaction with As(V) [89]. Consequently, we can deduce the As(V) adsorption mechanism was based on the ligand exchange between the As(V) with the sulfate anions or surface OH contained in α-FeOOH@GCA [89].

After degradation of ROX (curve A4 in Fig. 8A), the peaks at 878 cm^{-1} and 787 cm^{-1} assigned to the symmetric stretching vibration of As—O—Fe indicate the adsorption of As(V) degradation products onto the surface of α-FeOOH@GCA [87,88]. Compared with the ROX adsorption curve, many peaks in the aromatic rings of ROX completely disappear, which demonstrates the complete degradation of the adsorbed ROX. Curves A3 and A4 in Fig. 8A are almost the same except at the absorbance peaks at 878 cm^{-1} and 787 cm^{-1} due to different inner-sphere ligand complexes structure on α-FeOOH@GCA [89].

X-ray photoelectron spectra (XPS) address the same phenomena. Their O 1 s, Fe 2p, and As 3d spectra in α-FeOOH@GCA before and after degradation of ROX are shown in Fig. 8B–E.The characteristic peaks in wide scan spectrum before ROX degradation show up at binding energies of 284.8 eV (C 1s), 531.9 eV (O 1s), 711.7 eV (Fe 2p) and 168.8 eV (S 2p), confirming that the α-FeOOH@GCA contained C, O, Fe and S, respectively. The binding energy of 168.8 eV (S 2p) has the characteristic sulfate peaks shown to be present in the catalyst which maybe take part in the arsenic adsorption [90].

The deconvoluted O 1 s spectrum of pristine α-FeOOH@GCA has three main peaks with binding energies at 531.8, 533.2 and 530.6 eV. They can be assigned to the C–O-Fe bond formed between the GO and CNTs and α-FeOOH, to C—O linkages and to crystalline lattice oxygen in iron oxide [91–93]. Previously research [84] has identified the O 1 s of the C—O—Fe bond at 531–533 eV. This demonstrates the strong interfacial interactions between α-FeOOH and the GO-CNTs substrate, which further indicates that α-FeOOH is dispersed on the GO-CNTs substrate in a 3D structure. After ROX degradation, notice that the slight change of O 1s binding energy from 531.8 to 531.4 eV (Fe-O-As) was due to ligand exchange between formed As(V) and α-FeOOH@GCA.

The Fe 2p binding energy for the spin-orbit splitting peaks at 711.7 and 725.2 eV can be assigned to the Fe $2p_{3/2}$ of Fe(II) and Fe $2p_{1/2}$ of Fe (III) [94,95]. After ROX degradation, the new appearance of the deconvoluted binding energy at 715.2 eV corresponds to a broad Fe(II) satellite [96,97], indicating the reduction of Fe(III). The change in Fe 2p binding energy shows the efficient redox cycle of Fe(III) and Fe(II) on the catalyst surface in this system [34,46].

Compared with the spectrum of pristine α-FeOOH@GCA, the conspicuous rise in the peak intensity of As 3d at binding energy 45.6 eV in
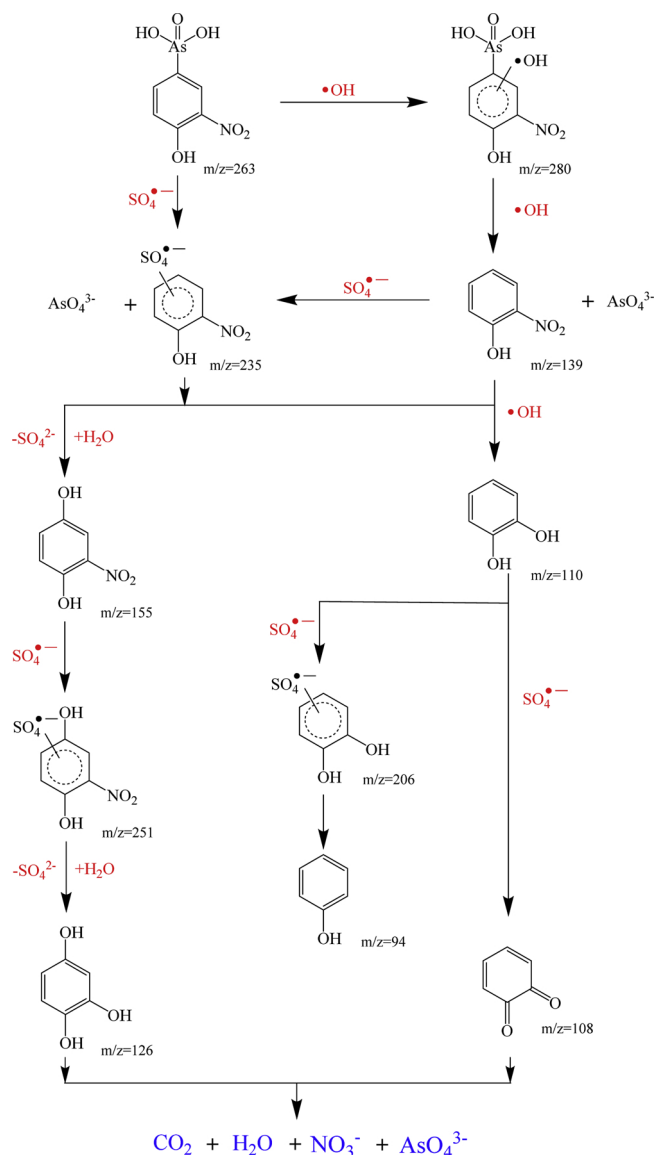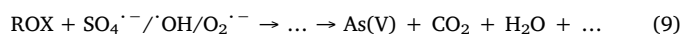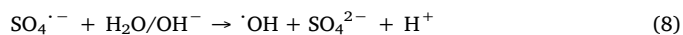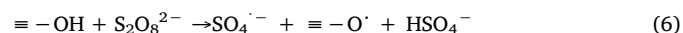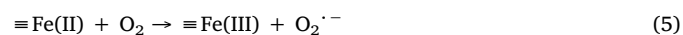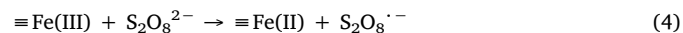
Scheme 1. Proposed ROX degradation pathway in the α-FeOOH@GCA/PS/UV system.

Fig. 8E [21,98] is attributable to As(V)-containing degradation products adsorbed on the catalyst's surface. We did not find the prescence of As (III) at binding energy 43.7 eV showing the strong oxidation in this system. This agrees well with the FTIR results and the results of the durability experiments. After the degradation of ROX by α-FeOOH@GCA, the surface concentrations of C, Fe and S have a slender decline shown in Table. S1, resulting from the adsorption of degradation by-products on α-FeOOH@GCA surface. The increasing concentration ratio of C/Fe from 27.47% to 28.52% can be attributed to adsorbed organic intermediates of ROX on α-FeOOH@GCA surface. Increase in C/S ratio growth from 65.24% to 99.34% demonstrated the reduction of S element content on the surface of catalyst, which was due to the anion-exchange reaction between SO_4^{2-} and formed As(V) from degradation of ROX. It demonstrated that the physical and chemical property of α-FeOOH@GCA has barely changed during this degradation reaction.

$$S_2O_8^{2-} + M^{n+} \rightarrow M^{n+1} + SO_4^{2-} + SO_4^{\cdot -} \qquad (2)$$
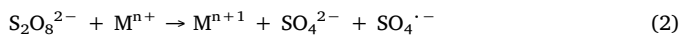
M here represents a transition metal such as iron, silver, copper or manganese [99]. One electron is transferred from the metal to the PS, which causes the formation of $SO_4^{\cdot -}$ radicals [54,100,101]. This study

has shown that PS can be activated by α-FeOOH@GCA to generate $SO_4^{\cdot -}$ through one electron transfer mechanism [102,103], At the same time, some $SO_4^{\cdot -}$ radicals react with OH- and H_2O in the solution to generate $^\cdot$OH and $O_2^{\cdot -}$ radicals [104,105]. The $SO_4^{\cdot -}$, $^\cdot$OH and $O_2^{\cdot -}$ radicals are mainly responsible for the oxidative degradation of ROX under UV irradiation. The redox cycle of Fe(III) and Fe(II) would be the rate-determining step in PS activation system. It is greatly enhanced by the introduction of GO-CNTs as the carrier of α-FeOOH and synergistic effect of α-FeOOH@GCA/PS/UV system. Eqs. (3)–(9) illustrate this proposed pathway. Here, ≡Fe(II) and ≡Fe(III) represent the iron oxidation states on the α-FeOOH@GCA surface, and Fe(II) and Fe(III) represent the iron ions in the solution [22,23].

$$\equiv Fe(II) + S_2O_8^{2-} \rightarrow \equiv Fe(III) + SO_4^{2-} + SO_4^{\cdot -} \qquad (3)$$

$$\equiv Fe(III) + S_2O_8^{2-} \rightarrow \equiv Fe(II) + S_2O_8^{\cdot -} \qquad (4)$$

$$\equiv Fe(II) + O_2 \rightarrow \equiv Fe(III) + O_2^{\cdot -} \qquad (5)$$

$$\equiv -OH + S_2O_8^{2-} \rightarrow SO_4^{\cdot -} + \equiv -O^\cdot + HSO_4^{-} \qquad (6)$$

$$S_2O_8^{2-} + h\nu \rightarrow 2\,SO_4^{\cdot -} \qquad (7)$$

$$SO_4^{\cdot -} + H_2O/OH^{-} \rightarrow {}^\cdot OH + SO_4^{2-} + H^{+} \qquad (8)$$

$$ROX + SO_4^{\cdot -}/{}^\cdot OH/O_2^{\cdot -} \rightarrow \dots \rightarrow As(V) + CO_2 + H_2O + \dots \qquad (9)$$

3.6. Recycling of As(v) as Ag₃AsO₄ catalyst

The As(V) formed from the oxidation of ROX in α-FeOOH@GCA/PS/UV system can be totally in-situ adsorbed by the catalyst given the optimum dose of α-FeOOH@GCA is used. The equilibrium adsorption capacity of As(V) on α-FeOOH@GCA can reach $112.4\,mg\,g^{-1}$ through Langmuir model fitting. The As(V) adsorption experiment is detailed in SI and the results are shown in Fig. S2. Usually, arsenic can be completely removed from the environment using adsorption techniques, but regeneration of the adsorbant then produces a large amount of arsenic-containing effluent. Disposing of it and recyling the As(V) must be safe and sustainable. In this study, the residual concentration of ROX almost can't be detected in either the solution or on the surface of the catalyst, and the adsorbed products retained on the catalyst were entirely As(V) oxyanions. This indicates that the As(V) derived from ROX degradation can be completely eliminated through α-FeOOH@GCA adsorption.

Ag₃AsO₄ particles were synthesised from the eluted arsenic using 0.1 M NaOH, as shown in Fig. 9A. The as-synthesized Ag₃AsO₄ was reddish-brown with nearly uniform submicron size of about 200 nm. The photocatalytic activity of Ag₃AsO₄ was studied through the degradation of seven organic contaminants listed in Fig. 9B and the fitting results of first-order model are shown in Table S1. The apparent first-order degradation rate of positively-charged MB and RhB was 0.086 (R^2 = 0.984) and $0.093\,min^{-1}$ (R^2 = 0.993), with neutral hydrophobic BPA and with 4-nitrophenol was 0.041 (R^2 = 0.859) and $0.053\,min^{-1}$ (R^2 = 0.982). The degradation of negatively-charged OII and OG and neutral hydrophilic phenol by Ag₃AsO₄ photocatalysis reached nearly 0.014 (R^2 = 1.00) and $0.016\,min^{-1}$ (R^2 = 0.990), 0.018 (R^2 = 0.886), respectively. Ag₃AsO₄ more easily degrade cationic dyes or hydrophobic organics than anionic dyes or hydrophilic organics probably due to the surface catalytic mechanism. It appears that Ag₃AsO₄ would be a promising degradation catalyst for a broad spectrum of organic contaminants. Scheme 2 presents a hypothetical scheme for the entire process.

4. Conclusion

In summary, the α-FeOOH@GCA/PS/UV system promises a sustainable way of integrating roxarsone degradation with recovery of the As(V) formed. It should have useful applicability in remediation of organoarsenics due to its fast degradation kinetics, efficiency and
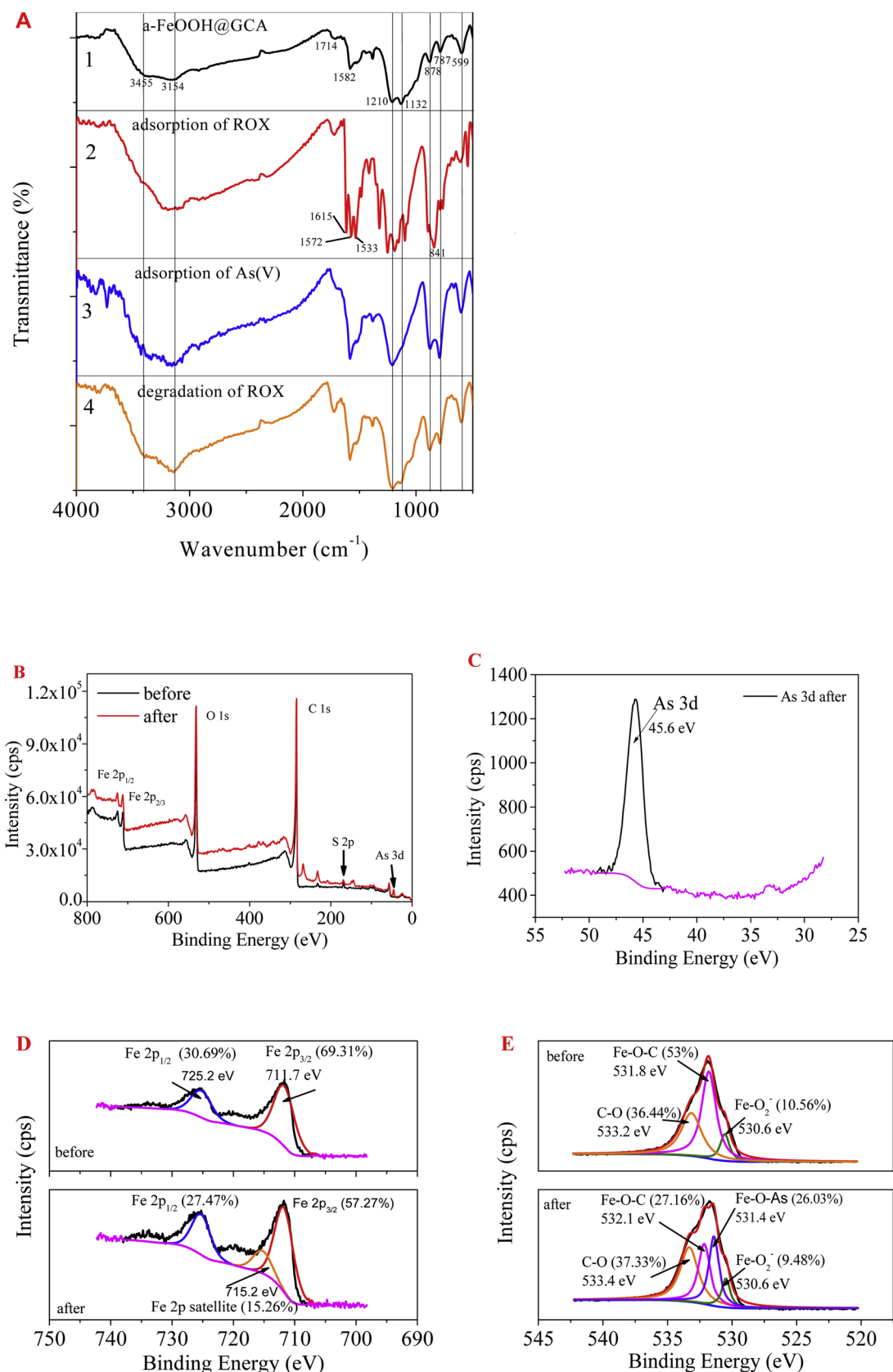
Fig. 8. FTIR spectra of α-FeOOH@GCA before or after degradation of ROX (A). XPS survey spectra of α-FeOOH@GCA (B) and core-level spectra of As 3d (C), Fe2p (D) and O1 s (E) before and after ROX degradation in the α-FeOOH@GCA/PS/UV system. A mechanism of PS activation through one-electron transfer involving a transition metal could be described as follows.
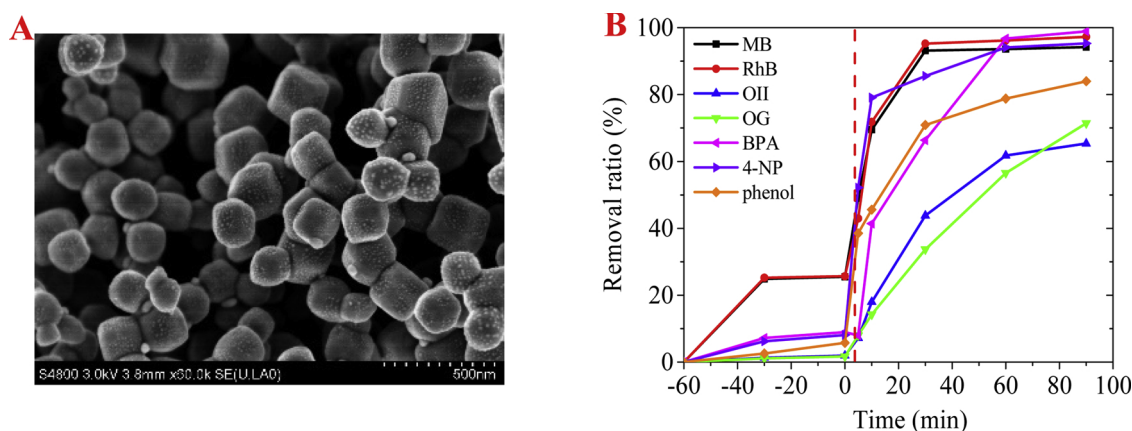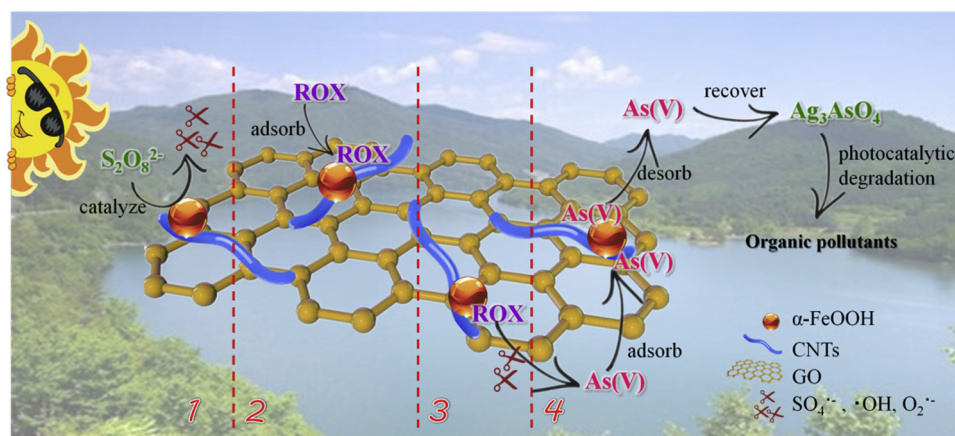
Fig. 9. (A) Scanning electron micrograph of the Ag$_3$AsO$_4$. (B) Photodegradation of various organic compounds by Ag$_3$AsO$_4$.

Scheme 2. A proposed mechanism for ROX degradation in the α-FeOOH@GCA/PS/UV system.

stability. The results indicate that ROX is adsorbed on the surface of the α-FeOOH@GCA and then attacked by sulfate, hydroxyl and superoxide radicals, resulting in the total conversion of As(V). Fe(II)/Fe(III) cycling on the surface of α-FeOOH@GCA is the dominant step in the one-electron transfer mechanism involved in PS activation. The As(V) degradation products can be recovered and used to form an excellent photocatalyst which shows good performance in the decomposition of a broad spectrum of environmental organic contaminants. This proposed system integrates ROX degradation with in-situ As(V) adsorption and As (V) recovery to form an excellent photocatalyst. It provides inspiration for the ultimate disposal of arsenic-containing compounds and a new perspective of further developing efficient arsenic-containing catalyst.

Notes

The authors declare no competing financial interest.

Appendix A. Supplementary data

Supplementary material related to this article can be found, in the online version, at doi:https://doi.org/10.1016/j.apcatb.2018.12.050.

References

[1] J.R. Garbarino, A.J. Bednar, D.W. Rutherford, R.S. Beyer, R.L. Wershaw, Environmental fate of roxarsone in poultry litter. I. Degradation of roxarsone during composting, Environ. Sci. Technol. 37 (2003) 1509–1514.

[2] X.D. Zhu, Y.J. Wang, C. Liu, W.X. Qin, D.M. Zhou, Kinetics, intermediates and acute toxicity of arsanilic acid photolysis, Chemosphere 107 (2014) 274–281.

[3] L.X. Yao, L.X. Huang, Z.H. He, C.M. Zhou, W.S. Lu, C.H. Bai, Delivery of roxarsone via chicken diet→chicken→chicken manure→soil→rice plant, Sci. Total Environ. 566 (2016) 1152–1158.

[4] J.L. Morrison, Distribution of arsenic from poultry litter in broiler chickens, soil, and crops, J. Agric. Food Chem. 17 (1969) 1288–1290.

[5] E.K. Silbergeld, K. Nachman, The environmental and public health risks associated with arsenical use in animal feeds, in: D.O. Carpenter (Ed.), Environmental Challenges in the Pacific Basin, Wiley-Blackwell, Malden, 2008, pp. 346–357.

[6] A. Islam, J.P. Maity, J. Bundschuh, C.Y. Chen, B.K. Bhowmik, K. Tazaki, Arsenic mineral dissolution and possible mobilization in mineral-microbe-groundwater environment, J. Hazard. Mater. 262 (2013) 989–996.

[7] I. Cortinas, J.A. Field, M. Kopplin, J.R. Garbarino, A.J. Gandolfi, R. Sierra-Alvarez, Anaerobic biotransformation of roxarsone and related N-substituted phenylarsonic acids, Environ. Sci. Technol. 40 (2006) 2951–2957.

[8] J.F. Stolz, E. Perera, B. Kilonzo, B. Kail, B. Crable, E. Fisher, M. Ranganathan, L. Wormer, P. Basu, Biotransformation of 3-nitro-4-hydroxybenzene arsonic acid (roxarsone) and release of inorganic arsenic by clostridium species, Environ. Sci. Technol. 41 (2007) 818–823.

[9] X. Xie, Y. Hu, H. Cheng, Rapid degradation of p-arsanilic acid with simultaneous arsenic removal from aqueous solution using fenton process, Water Res. 89 (2016) 59–67.

[10] J.B. Lin, S. Yuan, W. Wang, Z.-H. Hu, H.Q. Yu, Precipitation of organic arsenic compounds and their degradation products during struvite formation, J. Hazard. Mater. 317 (2016) 90–96.

[11] D. Arts, M.A. Sabur, H.A. Al-Abadleh, Surface interactions of aromatic orga-noarsenical compounds with hematite nanoparticles using ATR-FTIR: kinetic studies, J. Phys. Chem. A 117 (2013) 2195–2204.

[12] R. Datta, D. Sarkar, S. Sharma, K. Sand, Arsenic biogeochemistry and human health risk assessment in organo-arsenical pesticide-applied acidic and alkaline soils: an incubation study, Sci. Total Environ. 372 (2006) 39–48.

[13] A.A. Meharg, J. Hartley-Whitaker, Arsenic uptake and metabolism in arsenic

resistant and nonresistant plant species, New Phytol. 154 (2002) 29–43.

[14] D.J. Fisher, L.T. Yonkos, K.W. Staver, Environmental concerns of roxarsone in broiler poultry feed and litter in Maryland, USA, Environ. Sci. Technol. 49 (2015) 1999–2012.

[15] R. O'Connor, Transformations, air transport, and human impact of arsenic from poultry litter (vol 6, pg 83, 2005), Environ. Foren. 7 (2006) 101-101.

[16] F.M. Wang, Z.-L. Chen, L. Zhang, Y.-L. Gao, Y.-X. Sun, Arsenic uptake and accumulation in rice (oryza sativa l.) At different growth stages following soil incorporation of roxarsone and arsanilic acid, Plant Soil 285 (2006) 359–367.

[17] T. Lasky, W.Y. Sun, A. Kadry, M.K. Hoffman, Mean total arsenic concentrations in chicken 1989-2000 and estimated exposures for consumers of chicken, Environ. Health Perspect. 112 (2004) 18–21.

[18] L. Wang, H. Cheng, Birnessite (delta-MnO_2) mediated degradation of organoarsenic feed additive p-arsanilic acid, Environ. Sci. Technol. 49 (2015) 3473–3481.

[19] S. Zheng, W. Jiang, Y. Cai, D.D. Dionysiou, K.E. O'Shea, Adsorption and photocatalytic degradation of aromatic organoarsenic compounds in TiO_2 suspension, Catal. Today 224 (2014) 83–88.

[20] S. Li, J. Xu, W. Chen, Y. Yu, Z. Liu, J. Li, F. Wu, Multiple transformation pathways of p-arsanilic acid to inorganic arsenic species in water during UV disinfection, J. Environ. Sci. 47 (2016) 39–48.

[21] P. Hu, Y. Liu, B. Jiang, X. Zheng, J. Zheng, M. Wu, High-efficiency simultaneous oxidation of organoarsenic and immobilization of arsenic in fenton enhanced plasma system, Ind. Eng. Chem. Res. 54 (2015) 8277–8286.

[22] Q. Yang, H. Choi, Y. Chen, D.D. Dionysiou, Heterogeneous activation of peroxymonosulfate by supported cobalt catalysts for the degradation of 2,4-dichlorophenol in water: the effect of support, cobalt precursor, and UV radiation, Appl. Catal. B: Environ. 77 (2008) 300–307.

[23] P. Hu, M. Long, Cobalt-catalyzed sulfate radical-based advanced oxidation: a review on heterogeneous catalysts and applications, Appl. Catal. B: Environ. 181 (2016) 103–117.

[24] T. Olmez-Hanci, I. Arslan-Alaton, Comparison of sulfate and hydroxyl radical based advanced oxidation of phenol, Chem. Eng. J. 224 (2013) 10–16.

[25] S. Wacławek, H.V. Lutze, K. Grübel, V.V.T. Padil, M. Černík, D.D. Dionysiou, Chemistry of persulfates in water and wastewater treatment: a review, Chem. Eng. J. 330 (2017) 44–62.

[26] G.X. Huang, C.Y. Wang, C.W. Yang, P.C. Guo, H.Q. Yu, Degradation of bisphenol A by peroxymonosulfate catalytically activated with $Mn_{1.8}Fe_{1.2}O_4$ nanospheres: synergism between Mn and Fe, Environ. Sci. Technol. 51 (2017) 12600–12618.

[27] X. Du, Y. Zhang, I. Hussain, S. Huang, W. Huang, Insight into reactive oxygen species in persulfate activation with copper oxide: activated persulfate and trace radicals, Chem. Eng. J. 313 (2017) 1023–1032.

[28] Z. Jia, J. Kang, W.C. Zhang, W.M. Wang, C. Yang, H. Sun, D. Habibi, L.C. Zhang, Surface aging behaviour of Fe-based amorphous alloys as catalysts during heterogeneous photo fenton-like process for water treatment, Appl. Catal. B: Environ. 204 (2017) 537–547.

[29] S.X. Liang, Z. Jia, W.C. Zhang, X.F. Li, W.M. Wang, H.C. Lin, L.C. Zhang, Ultrafast activation efficiency of three peroxides by $Fe_{78}Si_9B_{13}$ metallic glass under photoenhanced catalytic oxidation: A comparative study, Appl. Catal. B: Environ. 221 (2018) 108–118.

[30] Z. Jia, X.G. Duan, P. Qin, Disordered atomic packing structure of metallic glass: toward ultrafast hydroxyl radicals production rate and strong electron transfer ability in catalytic performance, Adv. Funct. Mater. 27 (2017) 1–9.

[31] Z. Jia, W. Zhang, W. Wang, D. Habibi, L. Zhang, Amorphous $Fe_{78}Si_9B_{13}$ alloy: an efficient and reusable photo-enhanced fenton-like catalyst in degradation of cibacron brilliant red 3B-A dye under UV–vis light, Appl. Catal. B: Environ. 192 (2016) 46–56.

[32] D. Wang, R. Huang, W. Liu, D. Sun, Z. Li, Fe-based MOFs for photocatalytic CO_2 reduction: role of coordination unsaturated sites and dual excitation pathways, ACS Catal. 4 (2014) 4254–4260.

[33] D. Wang, F. Jia, H. Wang, F. Chen, Y. Fang, W. Dong, G. Zeng, X. Li, Q. Yang, X. Yuan, Simultaneously efficient adsorption and photocatalytic degradation of tetracycline by Fe-based MOFs, J. Colloid Interface Sci. 519 (2018) 273–284.

[34] Y. Song, Zero-valent iron activated persulfate remediation of polycyclic aromatic hydrocarbon-contaminated soils_ an in situ pilot-scale study, Chem. Eng. J. 355 (2019) 65–75.

[35] Y. Wang, Y. Gao, L. Chen, H. Zhang, Goethite as an efficient heterogeneous fenton catalyst for the degradation of methyl orange, Catal. Today 252 (2015) 107–112.

[36] Mem. Benacherine, N. Debbache, I. Ghoul, Y. Mameri, Heterogeneous photoinduced degradation of amoxicillin by goethite under artificial and natural irradiation, J. Photochem. Photobiol. A Chem. 335 (2017) 70–77.

[37] X. Shan, X. Guo, Y. Yin, Y. Miao, H. Dong, Surface modification of graphene oxide by goethite with enhanced tylosin photocatalytic activity under visible light irradiation, Colloids Surf. A: Physicochem. Eng. Aspects 520 (2017) 420–427.

[38] D.A. Jadhav, A.N. Ghadge, M.M. Ghangrekar, Enhancing the power generation in microbial fuel cells with effective utilization of goethite recovered from mining mud as anodic catalyst, Bioresour. Technol. 191 (2015) 110–116.

[39] K. Lin, J. Ding, H. Wang, X. Huang, J. Gan, Goethite-mediated transformation of bisphenol A, Chemosphere 89 (2012) 789–795.

[40] X. Li, Y. Huang, C. Li, J. Shen, Y. Deng, Degradation of pCNB by fenton like process using α-FeOOH, Chem. Eng. J. 260 (2015) 28–36.

[41] H. Liu, T. Chen, R.L. Frost, An overview of the role of goethite surfaces in the environment, Chemosphere 103 (2014) 1–11.

[42] J.H. Chen, H.T. Xing, H.X. Guo, W. Weng, S.R. Hu, S.X. Li, Y.H. Huang, X. Sun, Z.B. Su, Investigation on the adsorption properties of Cr(VI) ions on a novel graphene oxide (GO) based composite adsorbent, J. Mater. Chem. A 2 (2014)

[43] C.-Y. Lu, M.-Y. Wey, The performance of CNT as catalyst support on CO oxidation at low temperature, Fuel 86 (2007) 1153–1161.

[44] S. Park, J. An, J.R. Potts, A. Velamakanni, S. Murali, R.S. Ruoff, Hydrazine-reduction of graphite- and graphene oxide, Carbon 49 (2011) 3019–3023.

[45] L. Shi, X. Liu, Y. Tuo, J. Xu, P. Li, Y. Han, Graphene–CNT composite as catalyst support for microwave-assisted hydrogen releasing from liquid organic hydride, Int. J. Hydrogen Energy 42 (2017) 17403–17413.

[46] Y. Liu, X. Liu, Y. Zhao, D.D. Dionysiou, Aligned α-FeOOH nanorods anchored on a graphene oxide-carbon nanotubes aerogel can serve as an effective fenton-like oxidation catalyst, Appl. Catal. B: Environ. 213 (2017) 74–86.

[47] C. Liang, C.F. Huang, N. Mohanty, R.M. Kurakalva, A rapid spectrophotometric determination of persulfate anion in ISCO, Chemosphere 73 (2008) 1540–1543.

[48] H. Czili, A. Horváth, Applicability of coumarin for detecting and measuring hydroxyl radicals generated by photoexcitation of TiO_2 nanoparticles, Appl. Catal. B: Environ. 81 (2008) 295–302.

[49] W.A.M. Joseph Rabani, Max S. Matheson, The pulse radiolysis of aqueous tetranitromethane, J. Phys. Chem. 1966 (1965) 53–70.

[50] R.C. Hott, T.G. Andrade, M.S. Santos, A.C. Lima, M.C. Faria, C.A. Bomfeti, F. Barbosa, L.F. Maia, L.C. Oliveira, M.C. Pereira, J.L. Rodrigues, Adsorption of arsenic from water and its recovery as a highly active photocatalyst, Environ. Sci. Pollut. Res. Int. 23 (2016) 21969–21979.

[51] Y. Ma, Facile synthesis of α-FeOOH-γ-Fe_2O_3 by a pH gradient method and the role of γ-Fe_2O_3 in H_2O_2 activation under visible light irradiation, Chem. Eng. J. (2018) 75–84.

[52] Y. Wu, Composite of nano-goethite and natural organic luffa sponge as template_ synergy of high efficiency adsorption and visible-light photocatalysis, Inorg. Chem. Commun. 98 (2018) 115–119.

[53] J.A. Khan, X. He, N.S. Shah, H.M. Khan, E. Hapeshi, D. Fatta-Kassinos, D.D. Dionysiou, Kinetic and mechanism investigation on the photochemical degradation of atrazine with activated H_2O_2, $S_2O_8^{2-}$ and HSO_5^{-}, Chem. Eng. J. 252 (2014) 393–403.

[54] G. Fang, W. Wu, C. Liu, D.D. Dionysiou, Y. Deng, D. Zhou, Activation of persulfate with vanadium species for PCBs degradation: A mechanistic study, Appl. Catal. B: Environ. 202 (2017) 1–11.

[55] S. Yang, X. Yang, X. Shao, R. Niu, L. Wang, Activated carbon catalyzed persulfate oxidation of azo dye acid orange 7 at ambient temperature, J. Hazard. Mater. 186 (2011) 659–666.

[56] S. Jorfi, B. Kakavandi, H.R. Motlagh, M. Ahmadi, N. Jaafarzadeh, A novel combination of oxidative degradation for benzotriazole removal using TiO_2 loaded on $Fe^{II}Fe_2^{III}O_4$@C as an efficient activator of peroxymonosulfate, Appl. Catal. B: Environ. 219 (2017) 216–230.

[57] C. Tan, N. Gao, Y. Deng, J. Deng, S. Zhou, J. Li, X. Xin, Radical induced degradation of acetaminophen with Fe_3O_4 magnetic nanoparticles as heterogeneous activator of peroxymonosulfate, J. Hazard. Mater. 276 (2014) 452–460.

[58] Y. Tu, Y. Xiong, S. Tian, L. Kong, C. Descorme, Catalytic wet air oxidation of 2-chlorophenol over sewage sludge-derived carbon-based catalysts, J Hazard. Mater. 276 (2014) 88–96.

[59] Y. Wang, D. Cao, X. Zhao, Heterogeneous degradation of refractory pollutants by peroxymonosulfate activated by CoOx-doped ordered mesoporous carbon, Chem. Eng. J. 328 (2017) 1112–1121.

[60] C.J. Liang, C.J. Bruell, M.C. Marley, K.L. Sperry, Thermally activated persulfate oxidation of trichloroethylene (TCE) and 1,1,1-trichloroethane (TCA) in aqueous systems and soil slurries, Soil. Sediment. Contam. 12 (2003) 207–228.

[61] F. Chen, W. An, L. Liu, Y. Liang, W. Cui, Highly efficient removal of bisphenol A by a three-dimensional graphene hydrogel-AgBr@rGO exhibiting adsorption/photocatalysis synergy, Appl. Catal. B: Environ. 217 (2017) 65–80.

[62] D.H. Kim, A.D. Bokare, M.S. Koo, W. Choi, Heterogeneous catalytic oxidation of As (III) on nonferrous metal oxides in the presence of H_2O_2, Environ. Sci. Technol. 49 (2015) 3506–3513.

[63] J.B. Chen, W. Hong, T.Y. Huang, L.M. Zhang, W.W. Li, Y. Wang, Activated carbon fiber for heterogeneous activation of persulfate: implication for the decolorization of azo dye, Environ. Sci. Pollut. Res. 23 (2016) 18564–18574.

[64] L. Hu, G. Zhang, Q. Wang, Y. Sun, M. Liu, P. Wang, Facile synthesis of novel Co_3O_4-Bi_2O_3 catalysts and their catalytic activity on bisphenol A by peroxymonosulfate activation, Chem. Eng. J. 326 (2017) 1095–1104.

[65] J. Lv, Q. Hu, C. Cao, Y. Zhao, Modulation of valence band maximum edge and photocatalytic activity of BiOX by incorporation of halides, Chemosphere 191 (2017) 427–437.

[66] L. Tang, Y. Liu, J. Wang, G. Zeng, Y. Deng, H. Dong, H. Feng, J. Wang, B. Peng, Enhanced activation process of persulfate by mesoporous carbon for degradation of aqueous organic pollutants: electron transfer mechanism, Appl. Catal. B: Environ. 231 (2018) 1–10.

[67] L.J. Xu, J.L. Wang, Magnetic nanoscaled Fe_3O_4/CeO_2 composite as an efficient fenton-like heterogeneous catalyst for degradation of 4-chlorophenol, Environ. Sci. Technol. 46 (2012) 10145–10153.

[68] Z. Huang, Z. Bao, H. Yao, W. Lu, W. Chen, Novel green activation processes and mechanism of peroxymonosulfate based on supported cobalt phthalocyanine catalyst, Appl. Catal. B: Environ. 154-155 (2014) 36–43.

[69] M. Pu, Z. Guan, Y. Ma, J. Wan, Y. Wang, M.L. Brusseau, H. Chi, Synthesis of iron-based metal-organic framework MIL-53 as an efficient catalyst to activate persulfate for the degradation of Orange G in aqueous solution, Appl. Catal. A Gen. 549 (2018) 82–92.

[70] W. Han, W. Zhu, P. Zhang, Y. Zhang, L. Li, Photocatalytic degradation of phenols in aqueous solution under irradiation of 254 and 185 nm UV light, Catal. Today 90 (2004) 319–324.

[71] Y. Hou, J. Qu, X. Zhao, P. Lei, D. Wan, C.P. Huang, Electro-photocatalytic degradation of acid orange II using a novel TiO_2/ACF photoanode, Sci. Total Environ. 407 (2009) 2431–2439.

[72] J.R.G.A.J. Bednar, I. Ferrer, D.W. Rutherford, R.L. Wershaw, J.F. Ranville, T.R. Wildeman, Photodegradation of roxarsone in poultry litter leachates, Sci. Total Environ. 302 (2003) 237–245.

[73] H.A.A. Seed ahmed, H.C. Swart, R.E. Kroon, Investigating the capability of ToF-SIMS to determine the oxidation state of Ce, Phys. B: Condens. Matter (2017).

[74] S. Yang, P. Wang, X. Yang, G. Wei, W. Zhang, L. Shan, A novel advanced oxidation process to degrade organic pollutants in wastewater: microwave-activated persulfate oxidation, J. Environ. Sci. 21 (2009) 1175–1180.

[75] J.F. Boily, J. Szanyi, A.R. Felmy, A combined FTIR and TPD study on the bulk and surface dehydroxylation and decarbonation of synthetic goethite, Geochim. Cosmochim. Acta 70 (2006) 3613–3624.

[76] J.-F. Boily, A.R. Felmy, On the protonation of oxo- and hydroxo-groups of the goethite (α-FeOOH) surface: A FTIR spectroscopic investigation of surface O–H stretching vibrations, Geochim. Cosmochim. Acta 72 (2008) 3338–3357.

[77] G.Y. Zhang, D. Peak, Studies of Cd(II)–sulfate interactions at the goethite–water interface by ATR-FTIR spectroscopy, Geochim. Cosmochim. Acta 71 (2007) 2158–2169.

[78] S.J. Hug, In situ fourier transform infrared measurements of sulfate adsorption on hematite in aqueous solutions, J. Colloid Interface Sci. 188 (1997) 415–422.

[79] S. Kabiri, D.N.H. Tran, T. Altalhi, D. Losic, Outstanding adsorption performance of graphene–carbon nanotube aerogels for continuous oil removal, Carbon 80 (2014) 523–533.

[80] M. Ristić, S. Musić, M. Godec, Properties of γ-FeOOH, α-FeOOH and α-Fe_2O_3 particles precipitated by hydrolysis of Fe^{3+} ions in perchlorate containing aqueous solutions, J. Alloys Compd. 417 (2006) 292–299.

[81] L. Kuang, Y. Liu, D. Fu, Y. Zhao, FeOOH-graphene oxide nanocomposites for fluoride removal from water: acetate mediated nano FeOOH growth and adsorption mechanism, J. Colloid Interface Sci. 490 (2017) 259–269.

[82] X.M. Maria Pena, George P. Korfiatis, Chuanyong Jing, Adsorption mechanism of arsenic on nanocrystalline titanium dioxide, Environ. Sci. Technol. 40 (4) (2006) 1257–1262.

[83] X. Wang, Correlation between the adsorption ability and reduction degree of graphene oxide and tuning of adsorption of phenolic compounds, Carbon 69 (2014) 101–112.

[84] J. Taheri-Shakib, Experimental investigation of comparing electromagnetic and conventional heating effects on the unconventional oil (heavy oil) properties based on heating time and upgrading, Fuel 228 (2018) 243–253.

[85] S. Hu, D. Zhang, Y. Xiong, Y. Yang, Y. Ran, Nanopore-filling effect of phenanthrene sorption on modified black carbon, Sci. Total Environ. 642 (2018) 1050–1059.

[86] Y. Zhu, X. Cao, Y. Cheng, T. Zhu, Performances and structures of functional microbial communities in the mono azo dye decolorization and mineralization stages, Chemosphere 210 (2018) 1051–1060.

[87] Q. Hu, Y. Liu, X. Gu, Y. Zhao, Adsorption behavior and mechanism of different arsenic species on mesoporous $MnFe_2O_4$ magnetic nanoparticles, Chemosphere 181 (2017) 328–336.

[88] S.C. Sarah Depalma, Tuan Hoang, Hind A. Al-Abadleh, Adsorption thermodynamics of p-arsanilic acid on iron (oxyhydr)oxides: in-situ ATR-FTIR studies, Environ. Sci. Technol. 42 (6) (2008) 1922–1927.

[89] D. Fu, Z. He, S. Su, B. Xu, Y. Liu, Y. Zhao, Fabrication of alpha-FeOOH decorated graphene oxide-carbon nanotubes aerogel and its application in adsorption of arsenic species, J. Colloid Interface Sci. 505 (2017) 105–114.

[90] P.B.L.T. Weng, J.H. Stone-Masui, W.E.E. Stone, Desorption of emulsifiers from polystyrene latexes studied by various surface techniques: A comparison between XPS, ISS, and static SIMS, Langmuir 13 (1997) 2943–2952.

[91] P. Shao, J. Tian, B. Liu, W. Shi, S. Gao, Y. Song, M. Ling, F. Cui, Morphology-tunable ultrafine metal oxide nanostructures uniformly grown on graphene and their applications in the photo-fenton system, Nanoscale 7 (2015) 14254–14263.

[92] Y.X. Zhang, Y. Jia, A facile solution approach for the synthesis of akaganéite (β-FeOOH) nanorods and their ion-exchange mechanism toward As(v) ions, Appl. Surf. Sci. 290 (2014) 102–106.

[93] H. Song, L. Xia, X. Jia, W. Yang, Polyhedral α-Fe_2O_3 crystals@RGO nanocomposites: synthesis, characterization, and application in gas sensing, J. Alloys Compd. 732 (2018) 191–200.

[94] S.H. Zhang, M.F. Wu, T.T. Tang, Q.J. Xing, C.Q. Peng, F. Li, H. Liu, X.-B. Luo, J.-P. Zou, X.B. Min, J.M. Luo, Mechanism investigation of anoxic Cr(VI) removal by nano zero-valent iron based on XPS analysis in time scale, Chem. Eng. J. 335 (2018) 945–953.

[95] Y. Wang, J. Fang, J.C. Crittenden, C. Shen, Novel RGO/alpha-FeOOH supported catalyst for fenton oxidation of phenol at a wide pH range using solar-light-driven irradiation, J. Hazard. Mater. 329 (2017) 321–329.

[96] J. Du, J. Bao, C. Lu, D. Werner, Reductive sequestration of chromate by hierarchical FeS@Fe(0) particles, Water Res. 102 (2016) 73–81.

[97] Y. Gong, L. Gai, J. Tang, J. Fu, Q. Wang, E.Y. Zeng, Reduction of Cr(VI) in simulated groundwater by FeS-coated iron magnetic nanoparticles, Sci. Total Environ. 595 (2017) 743–751.

[98] Z.Z. Tianyi Sun, Zhijie Liang, Jie Liu, Wenxin Shi, Fuyi Cui, Efficient degradation of p-arsanilic acid with arsenic adsorption by magnetic CuO-Fe_3O_4 nanoparticles under visible light irradiation, Chem. Eng. J. 334 (2018) 1527–1536.

[99] Y. Li, Z. Yang, H. Zhang, X. Tong, J. Feng, Fabrication of sewage sludge-derived magnetic nanocomposites as heterogeneous catalyst for persulfate activation of Orange G degradation, Colloids Surf. A: Physicochem. Eng. Asp. 529 (2017) 856–863.

[100] G.P.A.D. Dionysiou, Radical generation by the interaction of transition metals with Common oxidants, Environ. Sci. Technol. 38 (2004) 3705–3712.

[101] C. Zhu, G. Fang, D.D. Dionysiou, C. Liu, J. Gao, W. Qin, D. Zhou, Efficient transformation of DDTs with persulfate activation by zero-valent iron nanoparticles: a mechanistic study, J. Hazard. Mater. 316 (2016) 232–241.

[102] L.W. Matzek, K.E. Carter, Activated persulfate for organic chemical degradation: a review, Chemosphere 151 (2016) 178–188.

[103] F. Ghanbari, M. Moradi, Application of peroxymonosulfate and its activation methods for degradation of environmental organic pollutants: review, Chem. Eng. J. 310 (2017) 41–62.

[104] H. Liu, T.A. Bruton, W. Li, J. Van Buren, C. Prasse, F.M. Doyle, D.L. Sedlak, Oxidation of benzene by persulfate in the presence of Fe(III)- and Mn(IV)-containing oxides: stoichiometric efficiency and transformation products, Environ. Sci. Technol. 38 (2004) 3705–3712.